Available online at www.sciencedirect.com
SCIENCE DIRECT®
Journal of Magnetic Resonance 181 (2006) 179–194
JMR Journal of Magnetic Resonance
www.elsevier.com/locate/jmr

Spatial encoding and the single-scan acquisition of high definition MR images in inhomogeneous fields

Assaf Tal, Lucio Frydman *

Department of Chemical Physics, Weizmann Institute of Science, 76100 Rehovot, Israel

Received 31 January 2006; revised 7 June 2006

Abstract

We have recently proposed a protocol for retrieving multidimensional magnetic resonance spectra and images within a single scan, based on a spatial encoding of the spin interactions. The spatial selectivity of this encoding process also opens up new possibilities for compensating magnetic field inhomogeneities; not by demanding extreme uniformities from the B_0 fields, but by compensating for their effects at an excitation and/or refocusing level. This potential is hereby discussed and demonstrated in connection with the single-scan acquisition of high-definition multidimensional images. It is shown that in combination with time-dependent gradient and radiofrequency manipulations, the new compensation approach can be used to counteract substantial field inhomogenities at either global or local levels over relatively long periods of time. The new compensation scheme could find uses in areas where heterogeneities in magnetic fields present serious obstacles, including rapid studies in regions near tissue/air interfaces. The principles of the B_0 compensation method are reviewed for one- and higher-dimensional cases, and experimentally demonstrated on a series of 1D and 2D single-scan MRI experiments on simple phantoms.

Keywords: MRI; Ultrafast imaging; Spatial encoding; Inhomogeneity compensation

1. Introduction

"Ultrafast" MRI methods such as echo-planar imaging (EPI), can afford multidimensional profiles of a sample in a non-invasive fashion and within a fraction of a second [1–6]. Like its Jeener–Ernst n-dimensional (nD) NMR spectroscopy counterpart [7,8] EPI relies on a Fourier transformation (FT) of the signals to extract the desired correlation between intervening Bohr precession frequencies. Unlike what is done in conventional 2D NMR spectroscopy, however, where the frequencies to be correlated occupy separate portions of the experiment, 2D EPI alternates the relative contributions of the frequencies defining the spins' evolution, so as to deliver the complete 2D time-domain interferogram following a single excitation of the spins. This "k-space walk" principle can be carried out by switching the intervening gradients or by modulating them concurrently, leading to a variety of related ultrafast acquisition modes [1–4,9–12]. In an effort to emulate EPIs advantages, we have recently proposed an alternative nD NMR acquisition scheme capable of affording arbitrarily high-dimensional data sets within a single scan [13–16]. The resulting "ultrafast" nD protocol is applicable both within a purely spectroscopic scenario or within an imaging-oriented one [16,17], and it relies on encoding the NMR interactions one is attempting to measure along an ancillary inhomogeneous frequency domain. This is most often introduced by the application of an external magnetic field gradient, which endows spins located at different positions with individually addressable frequencies. When applied in conjunction with a frequency-incremented excitation or inversion of the spins such gradients lead to the possibility of "spatially encoding" the NMR interactions to be measured. In other words, they allow one to encode an interaction Ω_1 with a phase $\phi(r) \approx C\Omega_1(r - r_0)$, rather than with the usual temporal encoding $\phi(t) \approx \Omega_1 t$. Patterns encoded

* Corresponding author. Fax: +972 8 9344123.
E-mail address: lucio.frydman@weizmann.ac.il (L. Frydman).

1090-7807/$ - see front matter © 2006 Elsevier Inc. All rights reserved.
doi:10.1016/j.jmr.2006.06.022

in such fashion can be subject to a mixing process and subsequently read out with the aid of an acquisition gradient, revealing their initial evolution frequencies according to echo positions arising at $k = -C\Omega_1$. Furthermore, subjecting this acquisition gradient to multiple oscillations allows one to monitor the action of a second, direct-domain set of NMR Hamiltonians. This multiple-readout feature opens up the possibility to collect multidimensional NMR correlations within a single scan, irrespective of the details of the NMR experiment under question.

In addition to enabling the acquisition of multidimensional NMR/MRI data sets within a single scan, the position-dependent encoding of the interactions just described opens up another possibility: the acquisition of high-resolution NMR spectra from bulk samples, even when these are subject to local or global inhomogeneities of the magnetic field. Indeed as we have illustrated in a purely spectroscopic scenario [18] the spatial encoding underlying ultrafast NMR can be exploited to correct, at the time of the spatially-dependent spin excitation, for the effects that field distortions will have at a later time when the signal acquisition will take place. Related compensation principles have also been demonstrated along direct acquisition domains with the introduction of so-called "shim pulses" [19]. These procedures do not entail a betterment of the fields but rather radio frequency (RF) manipulations, which can address either longitudinal (B_0) or transverse (B_1) field distortions by manipulations of the phase and/or amplitudes of the pulses. The purpose of the present exposition is to further describe the compensating potential of the spatial encoding principle within a purely imaging scenario, where it is positions rather than internal shifts that are being sought. In particular, we wish to demonstrate how ultrafast nD NMR and the inhomogeneity-compensating capabilities characterizing spatial encoding methods can be combined, to enable the acquisition of high-definition single-scan nD MRI images even when spins are subject to sizable $\Omega_{\mathrm{inh}}(\boldsymbol{r})$ spatial distortions of the ideal B_0 static NMR field.

In order to facilitate the visualization of how these complementary features come together, we begin by reviewing the principles of the spatial encoding methodology as applied to an ideal nD MRI scenario. We then proceed to describe the basis of the compensation procedure in 1D MRI, and conclude by sketching its extension to higher-dimensional single-scan experiments. All these theoretical treatments are accompanied with demonstrations of their validity, using 1D and 2D MRI experiments on simple phantoms.

2. Spatial encoding: single-scan nD MRI acquisitions in homogeneous fields

2.1. Spatial encoding in one dimension

We address first the simplest of imaging cases: the mapping of a spin-density profile ρ along a single axis z. Whereas in traditional Fourier methods, spins are homogeneously excited via the application of a single hard pulse (Fig. 1A), spatial encoding relies on imparting on the spins an initial spatially-dependent phase $\phi_{\mathrm{e}}(z)$. One possible way of achieving this is by exciting the spins using a frequency-chirped RF pulse, whose offset O is swept while in the presence of an excitation gradient $G_{\mathrm{e}}\hat{z}$ (Fig. 1B). This pulse will address spins sequentially according to their coordinate z at times $\tau(z)$ when the RF offset matches the spin's resonance frequency $\omega(z)$:

$$O[\tau(z)] = \omega(z) = \gamma G_{\mathrm{e}} z + \Omega_1 \tag{1}$$

Ω_1 being the site's chemical shift. For the simplest case of an offset being swept at a constant rate R between initial and final values O_i, O_f, the instant at which the RF will address spins at a coordinate z will be given by

$$\tau(z) = \frac{\Omega_1 + \gamma G_{\mathrm{e}} z - O_i}{R}. \tag{2}$$

As initially discussed within an imaging context by Kunz [20,21], this addressing can be used to impart a spatially-progressive $\pi/2$-like excitation of the spins—provided that the amplitude of the RF field γB_1 has been set to an appropriate value *vis-à-vis* the sweep rate R. The kind of sequential excitation that can then be imposed on the spins illustrated in Fig. 2, which shows how sweeping an RF field whose amplitude has been set as $\gamma B_1 \approx 0.25\sqrt{|R|}$ induces a series of time-incremented spin nutations starting from identical longitudinal states $\vec{M} = [0, 0, 1]$, and concluding with nearly transverse z-dependent magnetizations $\vec{M} = [\cos\phi_{\mathrm{e}}(z), \sin\phi_{\mathrm{e}}(z), 0]$. The overall position-dependent phases $\phi_{\mathrm{e}}(z)$ accumulated by different z-isochromats over the course of such sweep are also displayed in this Figure; they can be expressed (within an arbitrary phase constant) as

$$\phi_{\mathrm{e}}(z) = \phi_{\mathrm{RF}}[\tau(z)] + [\tau_p - \tau(z)]\cdot\omega(z) \tag{3}$$

where τ_{p} is the overall duration of the frequency chirped pulse, and

$$\phi_{\mathrm{RF}}[\tau(z)] = \int_0^{\tau(z)} [O_i + Rt']\mathrm{d}t' \tag{4}$$

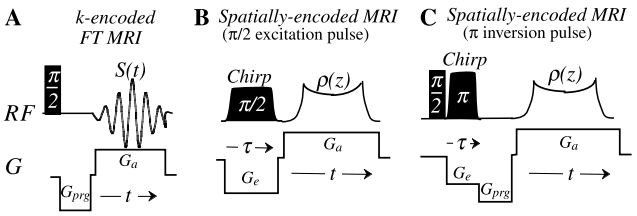

Fig. 1. Comparison of schemes capable of yielding MR profiles $\rho(z)$ from a 1D sample. (A) Conventional scheme where a gradient-driven k-domain $S(t)$ echo is monitored following a hard pulse, leading after FT to the 1D profile. (B) Non-FT scheme where positions are initially encoded via the application of a frequency-swept excitation pulse, and subsequently read out via the application of a decoding gradient. (C) *Idem* as (B) but with the encoding phase profile resulting from an adiabatic π-sweep which follows the initial hard-pulse excitation of the spins.

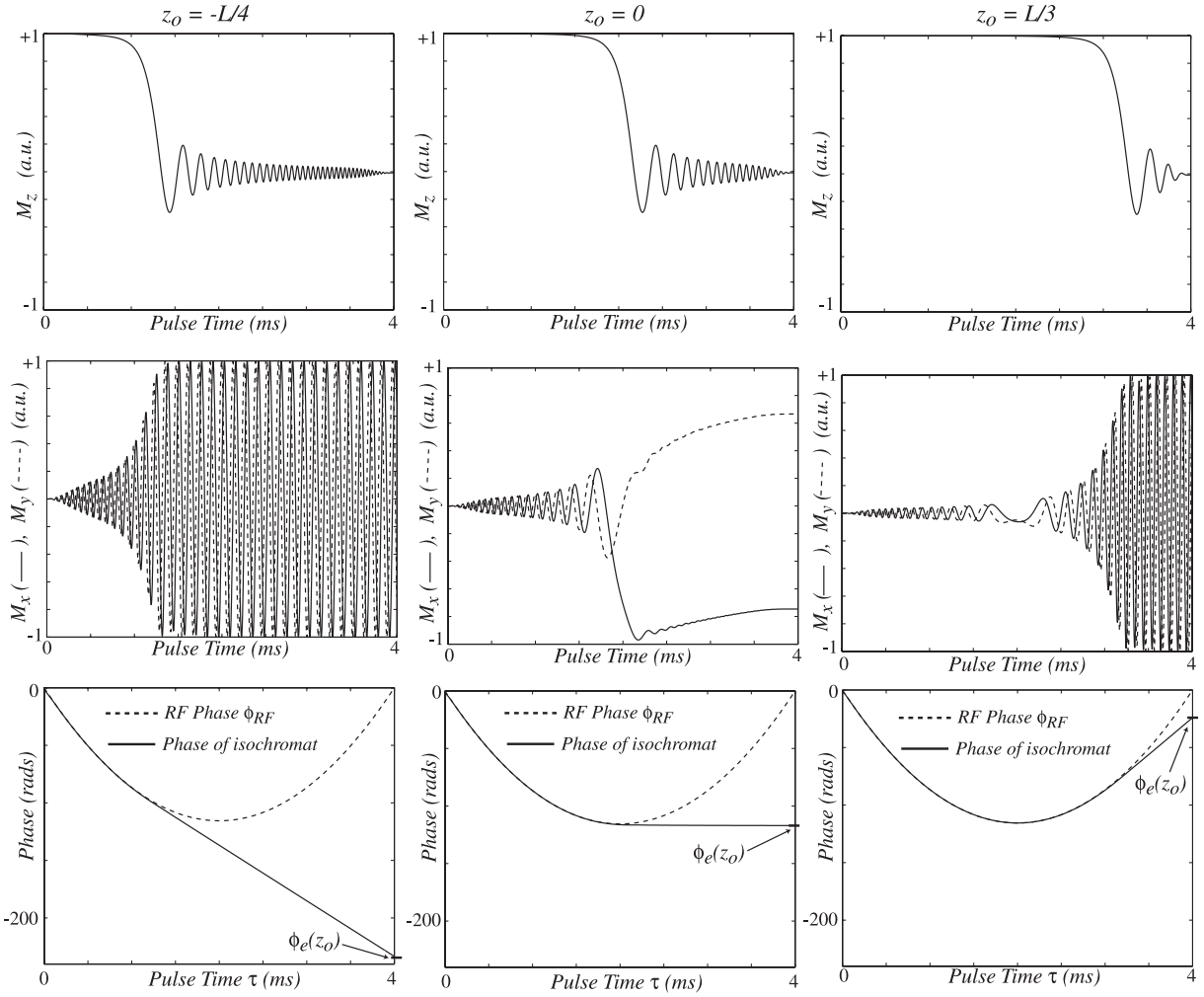

Fig. 2. Effects introduced by a chirped RF pulse on selected isochromats, positioned at the indicated fractional z_0 coordinates throughout a sample of length L. These simulations result from a numerical propagation of the Bloch equations with a 2 μs time resolution, and assumed a spatial encoding akin to that shown in Fig. 1B with the RF being swept at a constant rate over a range $\gamma_H G_e L = 36.8$ kHz while in the presence of a $G_e = 4$ G/cm gradient (i.e., sample length = 18 mm). Given a $\tau_p = 4$ ms pulse length the RFs amplitude was set at $\gamma B_1 = 0.25 \cdot \sqrt{36.8\ \text{kHz}/4\ \text{ms}} \approx 0.8$ kHz in order to achieve the desired $\pi/2$ nutations; notice the relatively sudden and nearly complete excitation then achieved by the pulse as a function of z. The lower panels illustrate the transverse phases accrued by the different isochromats as a result of the RF and gradient application; they verify the assumption given in Eq. (3), which describes the overall spin phase at the conclusion of τ_p as the sum of a quadratic component imparted by the RF (dotted parabola) plus a linear z-phase arising from free evolution under the action of the G_e gradient.

reflects the rotating-frame phase of the RF pulse at each instant $\tau(z)$. This contribution to ϕ_e is imparted onto spins positioned at any given coordinate z through the effects of the RF nutation, whereas the additional contribution to ϕ_e arises from the free evolution of the spins once they have been excited. The expression for ϕ_e can be further simplified by assuming an on-resonance single-site instance, and initial/final RF offsets chosen so as to excite a sample of physical length L. These two conditions can be summarized as

$$\Omega_1 = 0 \tag{5}$$

$$O_i = -O_f = -\gamma G_e L/2, \tag{6}$$

and lead to an overall phase encoding

$$\phi_e(z) = -\frac{\gamma G_e L \tau_p}{8} + \left(\frac{\gamma G_e \tau_p}{2}\right) z - \left(\frac{\gamma G_e \tau_p}{2L}\right) z^2. \tag{7}$$

This quadratic phase expression is analogous to that derived by Pipe [22,23], who exploited it in combination with a number of reconstruction algorithms to retrieve both spatial and angiographic images. By contrast to these quadratic reconstruction algorithms the single-scan nD NMR/MRI protocol delivers its spectral information via the application of a $G_a\hat{z}$ acquisition gradient, carrying out an analog FT

$$S(t) \propto \int_{\text{all } z} \mathrm{d}z\, \rho(z) \cdot \mathrm{e}^{\mathrm{i}\phi_e(z)} \mathrm{e}^{ik(t)\cdot z} \tag{8}$$

as a function of the extraction variable

$$k = \gamma \int_0^t G_a(t')\mathrm{d}t' = \gamma G_a t. \tag{9}$$

For a shift-free 1D MRI scenario where spins have been spatially-encoded as in Eq. (7), the resulting free induction

decay (FID) will then reflect signals from z coordinates fulfilling a stationary condition for the overall acquisition phase

$$\Phi(z,t) = \phi_e(z) + k(t)z. \tag{10}$$

In other words, the signal for any value $k(t)$ will arise only from those spins located at a z_k coordinate, such that

$$\frac{d}{dz}[\phi_e(z) + k(t)z]_{z=z_k} = 0. \tag{11}$$

Based on the expression in Eq. (7) for $\phi_e(z)$ there is only one solution to this condition, and it is:

$$z_k = \frac{L}{2} - \frac{R}{(\gamma G_e)^2}\cdot k(t). \tag{12}$$

Furthermore, for the case of this acquisition being implemented by a constant gradient applied over a time T_a chosen so as to unravel the full extent of the initial encoding (i.e., $G_a T_a = G_e\tau_p$), Eq. (12) can be simplified into

$$z_k(t) = \frac{L}{2} - \frac{L}{T_a}\cdot t. \tag{13}$$

The signal detected in this fashion can be explicitly described by expanding the overall acquisition phase around the relevant extremum:

$$\Phi(z) \approx \Phi(z_k) + \frac{1}{2}\left(\frac{d^2\Phi}{dz^2}\right)_{z=z_k}(z-z_k)^2. \tag{14}$$

Inserting this into Eq. (8) results in the FID

$$S(t) \propto e^{i\Phi(z_k)}\rho(z_k)\int_{z\approx z_k} dz \exp\left[i\left(\frac{d^2\Phi}{dz^2}\right)_{z=z_k}(z-z_k)^2/2\right] \tag{15}$$

which, relying on the identity

$$\int_{-\infty}^{\infty} dz e^{iaz^2} = \sqrt{\frac{\pi}{2|a|}}[1 + i\cdot\mathrm{sgn}(a)], \tag{16}$$

leads to a signal having an absolute value

$$|S(t)| \propto \sqrt{\frac{2\pi}{\left|\frac{d^2\Phi}{dz^2}\right|_{z=z_k}}}\rho(z_k). \tag{17}$$

Eqs. (13) and (17) mean that the time-domain signal will in this case probe the spins' density $\rho(z)$ in a one-to-one fashion, interrogating spins from the position that was excited last (assumed to be $z_f = L/2$) and walking its way "backwards" to the position that was first excited by the frequency chirp ($z_i = -L/2$). As for the weighting factor appearing in the collected FID,

$$\sqrt{\frac{2\pi}{\left|\frac{d^2\Phi}{dz^2}\right|_{z=z_k}}} = \sqrt{\frac{2\pi}{\left|\frac{d^2\phi_e}{dz^2}\right|_{z=z_k}}} = \frac{\sqrt{|2\pi R|}}{|G_e|}, \tag{18}$$

it defines the spatial extent Δz that will contribute to the signal of a particular $\rho(z_k)$ voxel or, in other words, it is the spatial resolution of the method. An important feature of this parameter is its independence on position z and on the acquisition variables k/t. This in turn is what guarantees that a constant point spread function will arise simply by monitoring the intensity of the FID signal as a function of time.

For the sake of completion, it is worth reviewing a second spatial encoding alternative, this one arising from the action of a frequency-swept π-pulse driving an *inversion* of the spins coming in the wake of an initial, homogeneous hard-pulse excitation (Fig. 1C). Following the arguments above as well as guidelines described elsewhere [24,25], one can estimate the overall encoding imparted during the course of such inversion pulse as

$$\phi_e(z) = -\tau_z\cdot\omega(z) + 2\phi_{RF}(\tau_z) + (\tau_p - \tau_z)\cdot\omega(z). \tag{19}$$

On comparing this expression with its analogue for the case of a frequency-chirped π/2 excitation (Eq. (3)) we notice an additional term $-\tau_z\omega(z)$ reflecting the encoding accumulated prior to the instant τ_z when the π inversion pulse reached an offset $\omega(z)$, and a doubling of the net ϕ_{RF} influence. Following the same assumptions as before ($\Omega_1 = 0$; $O_i = -O_f = -\gamma G_e L/2$; $R = \gamma G_e L/\tau_p$) this encoding phase can be written as[1]

$$\phi_e(z) = -\frac{\gamma G_e L\tau_p}{4} - \left(\frac{\gamma G_e\tau_p}{L}\right)z^2. \tag{20}$$

Main distinctions thus resulting between this π-driven encoding and that arising from its π/2 counterpart (Eq. (7)) include the absence of a linear term, and a doubling of the quadratic coefficient. The first of these features implies that upon imposing the stationary phase approximation the decoded positions will be given by

$$z[k(t)] = -\frac{2R}{(\gamma G_e)^2}\cdot k(t). \tag{21}$$

The initial position thus rasterized will correspond to the center of the sample, meaning that the full field-of-view (FOV) will be missed by the signal acquisition process unless an initial "purging" gradient pulse $k_{prg} = -\gamma G_e\tau_p/2$ is first applied. As for the second of these features it implies that, given identical conditions, the π-driven encoding will be characterized by a voxel size that is $\sqrt{2}$ time smaller (i.e., by a $\sqrt{2}$ higher resolution) than its π/2 encoding counterpart.

These expressions summarize the main features of spatially-encoded single-scan nD NMR, as applied to 1D MRI experiments. Fig. 3 exemplifies their experimental realization as applied to the profiling of a simple water phantom. Several features of this acquisition method had been presented in part in an earlier publication [17];[2] also compared there in further detail were issues concerning

[1] An analogous expression given earlier, Eq. (6b) in Ref. [24], mistakenly contains an additional $4\gamma G_e\tau_p z$ linear term.

[2] In that previous 2D-oriented publication, the encoding time $\tau_p - \tau$ was referred to as t_1 and the acquisition time t as t_2.

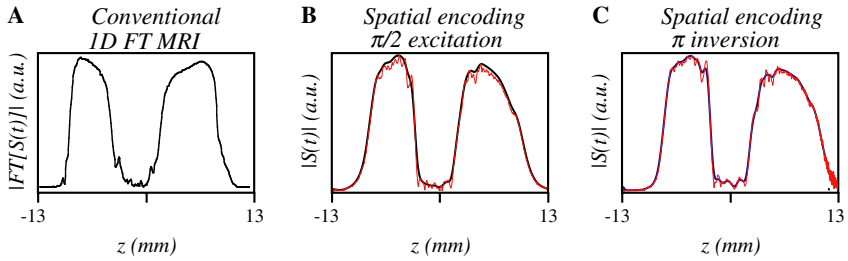

Fig. 3. Experimental illustration of the capability of the various pulse sequences introduced in Figs. 1A–C to afford 1D profiles of a sample. The phantom used in these experiments consisted of a uniform water-based polyacrylamide gel filling a 5 mm NMR tube, doped near its center with a $CoCl_2$ solution. The observation coil was nearly 18.5 mm in length, and the paramagnetic dope led to a low signal-intensity region ca. 3 mm long. Like all remaining experiments detailed in this study, these measurements were carried out at 501 MHz using a Varian iNOVA® NMR console. (A) Image arising by FT of an echo FID recorded under the action of a −5 G/cm longitudinal gradient, digitized over 5 ms using a 10 μs dwell time. A 2.5 ms long gradient pulse with $G_{prg} = 5$ G/cm and a 5 ms free evolution time (to enhance the T_2 contrast) were introduced prior to the acquisition. (B) Spatially-encoded images collected with $G_e = -G_a = 5$ G/cm, 5 ms long excitation (τ_p) and acquisition (T_a) times, and a 2 μs acquisition dwell time. A π/2 chirped RF pulse sweeping over ±21.5 kHz with an amplitude $\gamma B_1 \approx 750$ Hz was used for the spatial encoding, and a 5 ms free evolution delay was inserted prior to the actual data decoding. The image in red arose from taking the absolute value of the as-collected FID; the black image arose from subjecting the same data to a numerical filtering suited to $\gamma_a G_a \Delta z$ (rather than to $\gamma_a G_a L$) before the magnitude calculation. (C) *Idem* as in (B) but with the encoding arising from a 2.5 ms long, 1600 Hz strong π inversion pulse, applied following a hard-pulse excitation.

the overall sensitivities and demands on field gradients of the conventional *vis-à-vis* the spatially-encoded imaging approaches. It was then concluded that whereas the former could be made comparable by applying suitably matched filtering functions (black vs red profiles in Figs. 3B and C), conventional imaging makes a more efficient use of its excursion along the *k*-domain—monitoring signals from all voxels in the sample at once, rather than unraveling them in a voxel-by-voxel fashion. It follows that for a given number N_k of spatial elements, the wavenumber $k_{max} = \gamma G_a T_a$ to be used in the spatial encoding case has to exceed its conventional counterpart by a factor $\sqrt{N_k}$. This may often be a serious complication yet not always will it be an incapacitating one (for instance along the read-out dimension of a single-scan 2D EPI experiment); it is also possible that quadratic reconstruction algorithms [22,23] might also be of help to alleviate this feature. Yet another main difference between the methodologies is given by the built-in capabilities of the spatial encoding to compensate *experimentally* for field distortions, as further discussed in the last two Sections. Before going into this topic, however, we briefly describe how the 1D spatial encoding principle described in this Paragraph can be extended to single-scan acquisitions in multiple dimensions.

2.2. Spatially-encoded single-scan multidimensional MRI

Single-scan *n*D NMR relies on the fact that the spatial encoding procedure just described can deliver its information by the application of a field gradient. Since gradient effects can be reversed with nearly complete efficiency within arbitrarily short periods of time, spatial encoding enables one to monitor spectral distributions along multiple dimensions in a continuous "ultrafast" fashion. Such an extension to multiple dimensions does not necessarily imply that all domains to be explored need to be spatially encoded: performing the spatial encoding procedure along a given axis does not preclude the use of a conventional Fourier encoding along another orientation. Without attempting to present an exhaustive description of possibilities, Fig. 4 exemplifies this flexibility by presenting four different non-EPI approaches to the collection of 2D NMR images within a single scan. Also included in this Figure are cartoons depicting the different kinds of *r*/*k*-domain scannings that occur in each scheme. Fig. 4A presents a sequence where spins that have been spatially encoded along one axis, have their 1D profiles repeatedly rasterized during the course of the acquisition while another gradient incrementally "blips" their phases along an orthogonal domain. Fig. 4B is another *r*/*k*-encoding hybrid, where it is the spatial encoding dimension that now gets incrementally unraveled while the orthogonal axis is repeatedly imaged in reciprocal space via the application of a strong oscillatory gradient. Fig. 4C is a purely spatially-encoded 2D MRI possibility where orthogonal quadratic encoding phases are generated by frequency-swept excitation (π/2) and inversion (π) pulses, applied consecutively while under the action of corresponding gradients. Fig. 4D is another pure spatially-encoded alternative where a different quadratic pattern was generated by applying a pair of adiabatic π inversions following an initial homogeneous excitation, and the ensuing spatial encoding is subsequently unraveled in an out-spiraling fashion.

The hybrid cases depicted in Figs. 4A and B combine a unidimensional spatial encoding along one of the dimensions, with a conventional *k*-domain encoding along an orthogonal axis. The image formation process underlying these sequences can thus be directly derived from the unidimensional arguments given in the previous Paragraph, applied along orthogonal dimensions. Presented in Figs. 5A and B are experimental realizations of these two procedures, including for clarity some of the intermediate processing stages. Both of these experiments involved the continuous acquisition of a single-scan FID containing data in the mixed spatial–/wavenumber–domain (z, k_x); these data had to be suitably rearranged prior to further

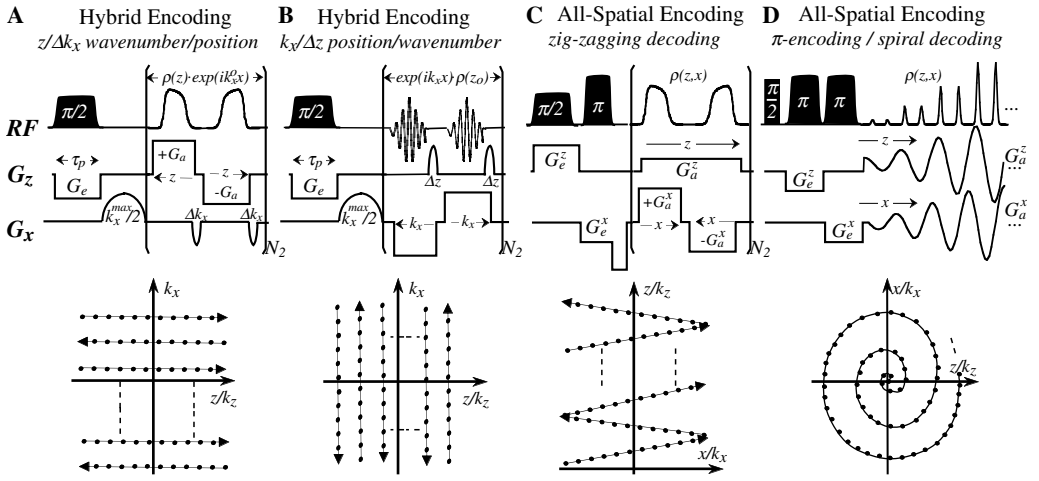

Fig. 4. Examples of different schemes that, with the aid of spatial encoding principles, can afford 2D MRI profiles within a single transient. (A) Hybrid scheme introduced in Ref. [17], relying on an initial G_e-driven encoding along one axis coupled to repetitive decoding echoes separated by small phase incrementations along the orthogonal direction. (B) Hybrid scheme were the roles of (A) have been reversed, and a single spatial decoding is interrupted by numerous repetitive k-domain acquisitions. (C) Purely spatial encoding alternative, where following an initial π/2-π encoding along orthogonal axes the image is rasterized along a zigzag trajectory. (D) Spatial encoding alternative whereby the profile is rasterized by an outward-expanding spiral trajectory. Shown for clarity are the k/r-space trajectories executed in each case, with dots representing the digitized data points.

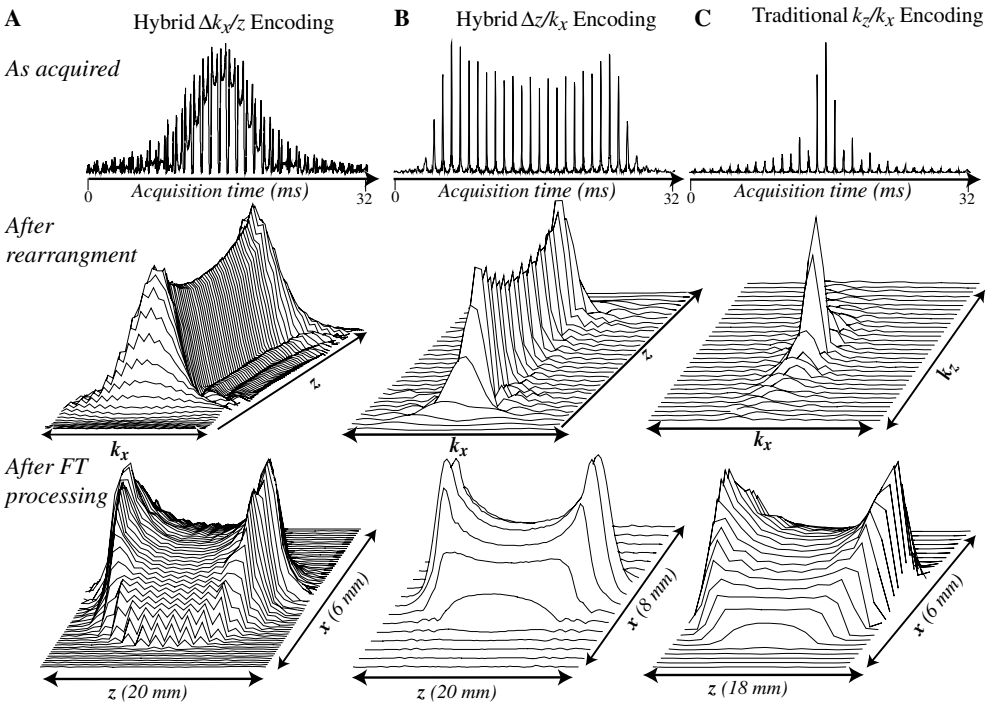

Fig. 5. Results obtained upon applying different single-scan 2D imaging protocols on a water-filled 5 mm NMR tube, with z representing the long axis of the sample. Shown on top are magnitude plots of the time-domain signal as collected in the spectrometer; the center row illustrates the same data after being correctly rearranged in their corresponding k/r spaces; plotted on the bottom are the 2D images arising from suitable FT (1D for A and B; 2D for C) of these rearranged data. (A) Experiment acquired using the hybrid $z/\Delta k_x$ encoding depicted in Fig. 4A with $G_e = 5$ G/cm, $\tau_p = 5$ ms, $k_x^{max} = 1.6$ mm^{-1}, $G_a = 26$ G/cm, $N_2 = 16$. (B) Experiment acquired using the hybrid $k_x/\Delta z$ encoding depicted in Fig. 4B with: $G_e = 5$ G/cm, $\tau_p = 5$ ms, $k_x^{max} = 1.6$ mm^{-1}, $N_2 = 16$, k_x scanning times of 950 μs, and Δz increments arising from pulsing 15 G/cm gradients over 50 μs. (C) 2D EPI experiment arising from a sequence akin to that in Fig. 4B except for the fact that the initial excitation preceded the first gradient and was given by a hard π/2 pulse; other acquisition parameters involved $G_e = 1$ G/cm, $\tau_p = 1$ ms, $k_x^{max} = 5.8$ mm^{-1}, $G_a^x = \pm 14.5$ G/cm, $G_a^z = 1.2$G/cm, $N_2 = 16$. In all experiments, data were digitized at 40 kHz.

processing. In the (A) case, this entailed a splicing of the individual z profiles, and their suitable rearrangement in a 2D matrix (including alternating reversals of the even/odd images) as a function of monotonically increasing k_x values. In (B), the $S(k_x)$ echoes were the ones which had to be spliced, reversed, and subsequently positioned in a

2D matrix as a function of a monotonically rasterized z coordinate. Finally, in both cases, a 1D FT along the k_x dimension—preceded and/or followed by suitable ancillary manipulations such as zero-filling, weighting, echo alignment procedures, magnitude calculations, etc.— are needed for obtaining the full 2D image. Presented for completion in Fig. 5C is a single-scan image collected using a traditional blipped k-space EPI encoding.

Figs. 4C and D present alternative approaches to single-scan 2D imaging, this time based entirely on spatial encoding principles. The first of these cases involves an initial $\pi/2$ excitation pulse chirped while in the presence of a $G_e^z\hat{z}$ gradient, followed by a π sweep executed while under the action of $G_e^x\hat{x}$. As a result of the spin inversion associated with the RF π pulse the total encoding then becomes a difference between Eqs. (20) and (7):

$$\phi_e(x,z) = \left[-\frac{\gamma G_e^x L_x \tau_p^x}{4} - \left(\frac{\gamma G_e^x \tau_p^x}{L_x}\right)x^2\right] - \left[-\frac{\gamma G_e^z L_z \tau_p^z}{8} + \left(\frac{\gamma G_e^z \tau_p^z}{2}\right)z - \left(\frac{\gamma G_e^z \tau_p^z}{2L_z}\right)z^2\right]. \quad (22)$$

Application of the EPI-type decoding scheme illustrated in Fig. 4C will thus yield an FID whose magnitude records the $\rho(x,z)$ sample profile *in real space*, starting from one end of the sample and then rastering the object along a zig-zag trajectory towards the opposite corner. Fig. 6A presents an experimental example of the corresponding image, once again collected for a simple cylindrical water phantom. Notice in it a "ribbed" structure along the z direction, associated to the relatively coarse zigzag chosen for this particular acquisition. By contrast to Eq. (22), the encoding procedure illustrated in Fig. 4D will result on the purely quadratic form

$$\phi_e(x,z) = \text{constant} - \left(\frac{\gamma G_e^x \tau_p^x}{L_x}\right)x^2 + \left(\frac{\gamma G_e^z \tau_p^z}{L_z}\right)z^2. \quad (23)$$

The initial $(x_0, z_o) = (0,0)$ coordinate at which the ensuing decoding will thus begin, makes this approach particularly well suited for a spiral-like decoding involving oscillating and time-incremented orthogonal gradients. Fig. 6B illustrates a phantom image obtained in this fashion. Notice that by no details regarding a coarse rasterization of the image are row evident. A point worth remarking again in connection to the spatially-encoded acquisitions displayed in Figs. 6A and B, is that no Fourier processing is needed for arriving to these single-scan 2D images. Therefore the absence of an equidistant grid of points within the bidimensional FIDs afforded by these spatially-encoded procedures constitutes a minor graphic-display inconvenience rather than, as is the case for FT-based k-domain acquisitions, an actual complication to be dealt with by numerical algorithms [1,2,26].

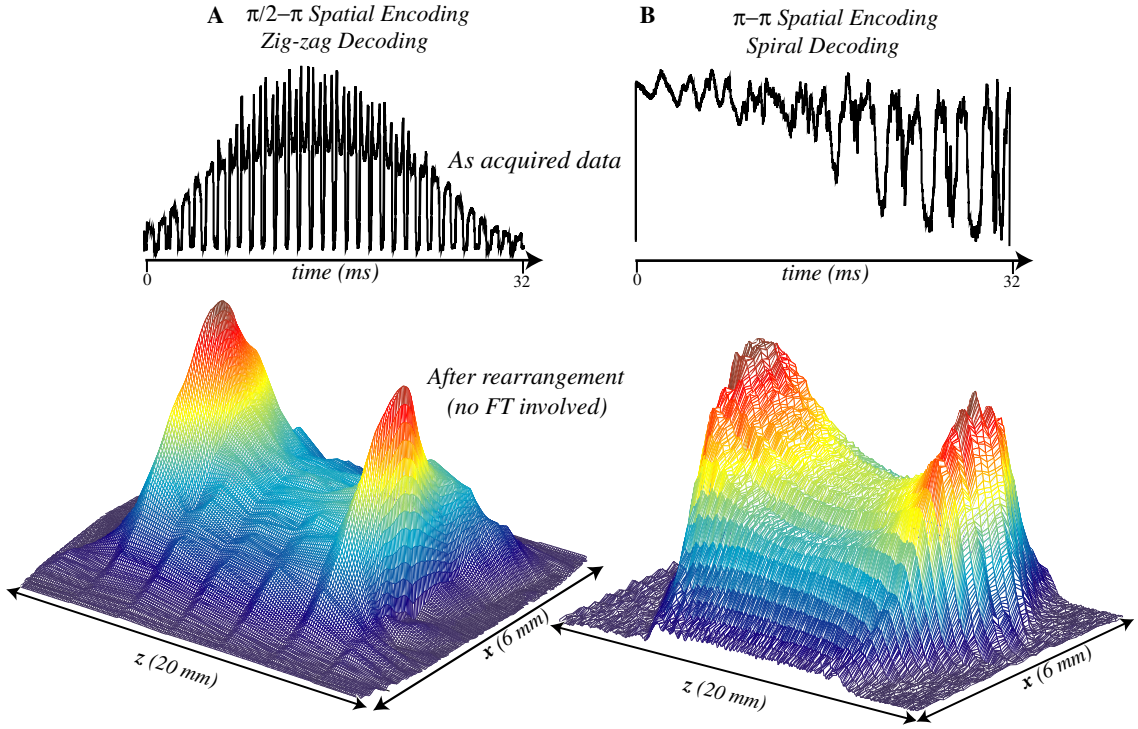

Fig. 6. Results obtained upon applying the purely spatial encoding single-scan 2D variants illustrated in Figs. 4C and D, to the same water profile exemplified in Fig. 5. Unlike those earlier examples only rearrangements of the collected data—no FTs—were involved in the image retrieval. The spatial encoding in (A) employed 5 ms $\pi/2$ and π chirped pulses applied in the presence of $G_e^z = 5$ G/cm, $G_e^x = 2.5$ G/cm, respectively; decoding used an effective $G_a^x = 0.4$ G/cm, $G_a^z = 25$ G/cm, $N_2 = 16$. The spatial encoding in (B) was imposed (along both axes) by applying 5 ms long adiabatic π pulses while in the presence of 4 G/cm gradients; the decoding involved eight gradient oscillations reaching to a maximum of 15 G/cm. Notice in this latter case the absence of the clear (x,z) profiles observed in (A)'s 1D time-domain signal, as well as of the "ribs" characterizing the 2D image in (A) along the z axis.

Fig. 6 exemplifies just two out of the numerous strategies by which purely spatially-encoded MRI procedures could be used to retrieve multidimensional images. Other possibilities—involving two or three dimensions, $\pi/2$ or π encoding pulses, etc.— can also be conceived. Assuming an ideal decoherence-free spin system, the in-plane rotating-frame magnetization patterns arising prior to the signal acquisition from any of these encoding procedures will be given by

$$M_{xy}(\boldsymbol{r}) = \rho(\boldsymbol{r})\mathrm{e}^{\mathrm{i}\phi_{\mathrm{e}}(\boldsymbol{r})}, \tag{24}$$

where

$$\phi_{\mathrm{e}}[\boldsymbol{r} = (x, y, z)] = \sum_{\alpha=x,y,z} \left(a_\alpha + b_\alpha \cdot \alpha + c_\alpha \cdot \alpha^2\right) \tag{25}$$

is a quadratic excitation phase encoded by the action of chirped pulses along the multiple spatial dimensions. In parallel to Eq. (8), the FID arising upon such pattern while executing a multidimensional "walk" through $\boldsymbol{k}$-space,

$$S(t) \propto \int_{\text{all } \boldsymbol{r}} \int \int \mathrm{d}\boldsymbol{r}\rho(\boldsymbol{r}) \cdot \mathrm{e}^{\mathrm{i}\phi_{\mathrm{e}}(\boldsymbol{r})}\mathrm{e}^{\mathrm{i}\boldsymbol{k}(t)\cdot\boldsymbol{r}}, \tag{26}$$

will reflect the rasterized $\rho(\boldsymbol{r})$ spatial profile of the spins. The particular coordinate $\boldsymbol{r}_{k(t)}$ decoded for a given $\boldsymbol{k}(t)$ value, will be the one fulfilling the 3D stationary phase condition

$$\nabla_{\boldsymbol{r}}[\phi_{\mathrm{e}}(\boldsymbol{r}) + \boldsymbol{k}(t) \cdot \boldsymbol{r}]_{\boldsymbol{r}=\boldsymbol{r}_k} = (0, 0, 0) \Longleftrightarrow \tag{27a}$$

$$k_\alpha = -b_\alpha - 2c_\alpha \cdot \alpha. \tag{27b}$$

An extension of the one-dimensional Taylor-expansion arguments given for the 1D case (Eq. (15)) can also yield the spatial resolution of the ensuing $|S(t)|\ \alpha\rho(\boldsymbol{r}_k)$ voxel element. In the 3D case, this will be related to the determinant of the Hessian matrix

$$\left\{Q_{ij} = D_{ij}[\phi_{\mathrm{e}}(r) + k(t) \cdot r]\right\}_{i,j=x,y,z}; \tag{28a}$$

$$D = \begin{pmatrix} \partial^2/\partial x^2 & \partial^2/\partial x\partial y & \partial^2/\partial x\partial z \\ \partial^2/\partial y\partial x & \partial^2/\partial y^2 & \partial^2/\partial y\partial z \\ \partial^2/\partial z\partial x & \partial^2/\partial z\partial y & \partial^2/\partial z^2 \end{pmatrix}, \tag{28b}$$

when evaluated at the particular coordinate $\boldsymbol{r}_k$. Based on Eq. (27a) this yields

$$|S(t)| \propto \sqrt{\frac{(2\pi)^3}{|\det(\boldsymbol{Q})|_{\boldsymbol{r}=\boldsymbol{r}_k}}}\rho(\boldsymbol{r}_k) \tag{29a}$$

$$= \prod_{\alpha=x,y,z} \sqrt{\frac{\pi}{|c_\alpha|}}\rho(\boldsymbol{r}_k). \tag{29b}$$

Unidimensional arguments can also be extended in a straightforward fashion to derive the FOVs along the independent axes, as well as to compare the demands that purely spatially-encoded *vis-à-vis* traditional EPI-encoding make in terms of gradient strengths, etc. Yet rather than continuing with these extensions we turn to the central topic of how to integrate field inhomogeneity compensations into the spatial encoding procedure.

3. Spatially-encoded 1D MRI in the presence of field inhomogeneities

3.1. Compensating for field inhomogeneities

For the sake of simplicity we begin by describing the retrieval of undistorted one-dimensional $\rho(z)$ profiles in the presence of field inhomogeneities, leaving for the last Section an extension to higher-dimensional cases. Fig. 7 illustrates experimentally the actual capabilities of the approach, comparing for a simple water phantom results obtained in the presence and absence of inhomogeneities, when utilizing both conventional and spatially-encoded 1D MRI approaches under similar gradient-strength conditions. Upon executing either one of the imaging procedures described in the previous Section while under the action of similar B_0 inhomogeneities, all methods will fail to deliver faithful representations of the object. The distortions imparted by these inhomogeneities onto the Fourier- and spatially-encoded images will, as expected, be different. And while ideally such distortions could be accounted for at a post-acquisition level via numerical compensation procedures [1,27,28], these compensations tend to be numerically unstable and therefore restricted under limited signal-to-noise conditions. On the other hand, owing to the voxel-by-voxel encoding and read-out involved in the spatial encoding procedures introduced in the previous Section, the latter have a built-in capability of restoring *at an experimental level* the faithfulness of the collected image. This capability is illustrated by the trace in Fig. 7E, collected using the same average gradient strength as the profile in Fig. 7D, but following a suitable temporal shaping of the RF encoding pulse and of the subsequent decoding gradient. Such shaping does actually require an *a priori* knowledge of the field inhomogeneity profile $\gamma\Delta B_0(z) = \Omega_{\mathrm{inh}}(z)$; yet given this knowledge the procedure can compensate distortions using gradients whose span is only a few times larger than the inhomogeneities—ca. a factor of four for the case illustrated in Fig. 7.

Recording such undistorted $\rho(z)$ profiles while in the presence of field inhomogeneities, will require restoring the two basic conditions which defined the ideal spatial-encoded image formation process: *a linearity between coordinate z and the acquisition time t* (Eq. (13)), and *a constant pixel size* Δz *throughout the acquisition process* (Eq. (18)). The physics that define these two parameters will not change fundamentally upon going from a homogeneous- to an inhomogeneous-field acquisition; voxels will still be decoded according to the stationary phase condition

$$\left.\frac{\mathrm{d}\Phi}{\mathrm{d}z}\right|_{z=z_{k(t)}} = 0, \tag{30}$$

and spatial resolution will still be defined by

$$\Delta z(t) = \sqrt{\frac{2\pi}{\left|\frac{d^2\Phi}{dz^2}\right|_{z=z_{k(t)}}}}. \tag{31}$$

The effects of the field inhomogeneities will be expressed by the fact that there will now be an additional contribution defining the overall phase $\Phi(z)$ arising from $\Omega_{\mathrm{inh}}(z)$—effects which will have to be compensated out. To visualize how this distortion can be removed we will assume for concreteness that spins were excited by the action of a swept $\pi/2$ chirped RF nutation.[3] The $\Omega_{\mathrm{inh}}(z)$ contribution will be given by an extra term in the excitation phase

$$\phi_{\mathrm{e}}(z) = \phi_{\mathrm{RF}}[\tau(z)] + [\tau_{\mathrm{p}} - \tau(z)]\cdot[\gamma G_{\mathrm{e}} z + \Omega_1 + \Omega_{\mathrm{inh}}(z)] \tag{32}$$

as well as by an addition to the overall acquisition phase

$$\Phi(z,t) = \phi_{\mathrm{e}}(z) + k\cdot z + \Omega_{\mathrm{inh}}(z)t. \tag{33}$$

If the encoding and decoding processes were to proceed as in the homogeneous case it is clear that these new terms would break both the linear z/t relation as well as the constant voxel size demand, leading to distortions such as those illustrated in Fig. 7D. Yet we can "force" a reintroduction of the ideal behavior by tailoring at least two of the several free parameters at our disposal; these include $\phi_{\mathrm{RF}}[\tau(z)]$ (i.e., the shape of the RF encoding pulse), $k(t)$ (i.e., the shape of the acquisition gradient G_{a} and/or of the dwell time Δt), as well as the encoding gradient G_{e}. In the present exposition, we have chosen $\phi_{\mathrm{RF}}[\tau(z)]$ and $G_{\mathrm{a}}(t)$, in order to carry out the corrections.

The demand for a linearity between z and t can be used to derive the shape of the acquisition gradient. To do so we insert Eq. (33) into expression 30, and solve for $\gamma G_{\mathrm{a}}(t) = \mathrm{d}k/\mathrm{d}t$

$$\gamma G_{\mathrm{a}}(t) = \left\{ -\frac{\mathrm{d}}{\mathrm{d}t}\left[\frac{\mathrm{d}\phi_{\mathrm{e}}(z)}{\mathrm{d}z}\right] - t\cdot\frac{\mathrm{d}}{\mathrm{d}t}\left[\frac{\mathrm{d}\Omega_{\mathrm{inh}}(z)}{\mathrm{d}z}\right] - \frac{\mathrm{d}\Omega_{\mathrm{inh}}(z)}{\mathrm{d}z}\right\}_{z=z(t)}, \tag{34}$$

The t-dependence in this expression can be translated into a z-dependence (or vice versa) by imposing the demand

$$z(t) = \frac{L}{2} - \frac{L}{T_{\mathrm{a}}}\cdot t \Longleftrightarrow \frac{\mathrm{d}}{\mathrm{d}t} = -\frac{L}{T_{\mathrm{a}}}\frac{\mathrm{d}}{\mathrm{d}z}, \tag{35}$$

which transforms Eq. (34) into a single-variable second-order differential expression. Although $\Omega_{\mathrm{inh}}(z)$ is an *a priori* mapped function, solving Eq. (34) still requires knowledge of the $\phi_{\mathrm{e}}(z)$ function—or better said, of its second spatial derivative—appearing on the first right-hand term. The definition of this function will stem in turn from demanding a constant pixel size throughout the acquisition. In other words, we shall design the initial encoding experienced by the spins during their excitation in such a way, so that when coupled to the cumulative dephasing effects of $\Omega_{\mathrm{inh}}(z)$ the overall result will be a time-independent Δz throughout the course of the acquisition. It follows from

[3] The description for the case of a π-based encoding follows very similar (and in fact somewhat simpler) lines.

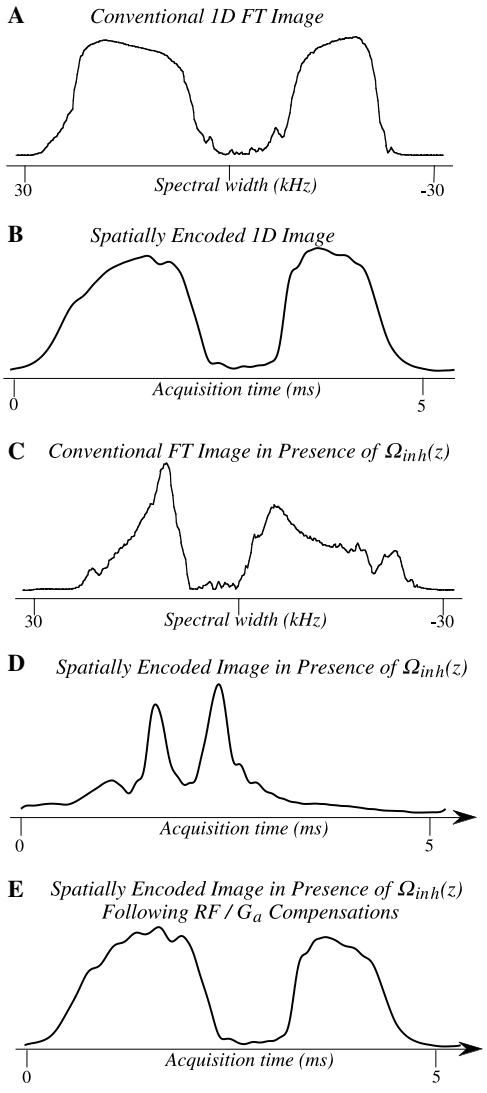

Fig. 7. Experimental demonstration of the field-compensating principles described in this work, for the case of the 1D phantom introduced in Fig. 3. (A and B) FT and spatially-encoded profiles collected from the phantom under conditions similar to those detailed in that Figure: 5 G/cm excitation and acquisition gradients, 10 ms average free-evolution times, 18.5 mm long samples, etc. (C and D) *Idem* as in (A and B), but upon subjecting on the sample an artificial $\Omega_{\mathrm{inh}}(z) = 1.31z - 0.193z^2$ kHz (with z the displacement away from the sample's center in mm). This inhomogeneity was introduced by distorting the z, z^2 magnet shims, and was characterized by mapping the water resonance using a simple gradient-echo sequence. (E) Idem as in (D) but after inserting the mapped inhomogeneity profile into the algorithm described in the text, recalculating from it the correcting RF sweep and acquisition gradient patterns, and applying these for the acquisition of the data. The most remarkable feature of this compensation procedure (and therefore a basic test of its correct functioning) is the fact that it enabled the signal to perdure in the time domain, long after either the conventional k-space or its analogous spatially-encoded signal have both decayed into the background noise. This, in spite of Ω_{inh} spanning over 25 kHz and of the experiment still requiring $G_{\mathrm{e}} = -5$ G/cm, and an average $G_{\mathrm{a}} = +4.13$ G/cm over the acquisition. Notice that although still not ideal, the "wiggles" exhibited by this experimental Ω_{inh}-compensated profile are akin to those of its homogeneous counterpart in (B). Simulations indicate that these reflect in both cases limitations of the chirped excitation pulse in delivering the desired profile, rather than in an actual failure of the compensation procedure.

Eq. (31) that such constant-voxel demand is mathematically equivalent to requesting

$$\frac{\mathrm{d}}{\mathrm{d}t}\left[\frac{\mathrm{d}^2\Phi(z)}{\mathrm{d}z^2}\right]_{z=z(t)} = 0. \tag{36}$$

Inserting into this expression the definitions given in Eqs. (33) and (35), results in demanding that $\phi_e(z)$ and $\Omega_{inh}(z)$ be related by

$$\frac{\mathrm{d}^3\phi_e(z)}{\mathrm{d}z^3} = -\frac{T_a}{L}\left[\frac{\mathrm{d}^2\Omega_{inh}(z)}{\mathrm{d}z^2} + (z-\frac{L}{2})\frac{\mathrm{d}^3\Omega_{inh}(z)}{\mathrm{d}z^3}\right]. \tag{37}$$

Notice that according to this derivation, the voxel size correction: (i) is introduced at an excitation but not at an acquisition level; (ii) will not be needed if Ω_{inh}'s effects are linear (which would introduce a constant displacement of the image but no intra-voxel distortions); (iii) will only affect third and higher orders of $\phi_e(z)$ (terms which were absent in the homogeneous case, Eq. (7)); and (iv) will allow by a single integration for the calculation of the acquisition gradient$G_a(t)$, pending certain simple boundary conditions that we proceed to discuss.

Eq. (37) defines the encoding profile that we would like applied on the spins, as a function of their z positions. This $\phi_e(z)$ profile depends on fixed parameters we shall assume known (G_e, Ω_1 and $\Omega_{inh}(z)$ in Eq. (32)), as well as on an RF-driven phase $\phi_{RF}[\tau(z)] = \int_0^{\tau(z)} O(\tau')\mathrm{d}\tau'$. This spatially-dependent phase profile we can control in a number of ways; for example by defining the instant $\tau(z)$ at which a particular RF offset O being continuously swept reaches and excites spins resonating at a frequency $\omega(z) = \gamma G_e z + \Omega_1 + \Omega_{inh}(z)$. To visualize how the resulting $O(\tau)$ sweep provides sufficient flexibility to design the desired $\phi_e(z)$ profile, we shall assume for simplicity a null chemical shift. Taking then the spatial derivative of Eq. (32) (as constant phase terms in the end are unimportant) one ends up with

$$\frac{\mathrm{d}\phi_e(z)}{\mathrm{d}z} = O[\tau(z)]\cdot\frac{\mathrm{d}\tau}{\mathrm{d}z} + [\tau_p - \tau(z)]\left[\gamma G_e + \frac{\mathrm{d}\Omega_{inh}(z)}{\mathrm{d}z}\right] - \frac{\mathrm{d}\tau}{\mathrm{d}z}\cdot[\gamma G_e + \Omega_{inh}(z)]. \tag{38}$$

Since the offset also has to fulfill the condition $O[\tau(z)] = \gamma G_e z + \Omega_{inh}(z)$, the first and last terms on the right-hand side of this expression will cancel each other out; one can then solve for $\tau(z)$ as

$$\tau(z) = \tau_p - \frac{\frac{\mathrm{d}\phi_e(z)}{\mathrm{d}z}}{\left[\gamma G_e + \frac{\mathrm{d}\Omega_{inh}(z)}{\mathrm{d}z}\right]}. \tag{39}$$

The expression for $\mathrm{d}\phi_e/\mathrm{d}z$ involved in this equation can be obtained from the $\Omega_{inh}(z)$ profile following a double integration of Eq. (37), subject to the initial and final boundary conditions of the RF sweep

$$\tau(z_f = L/2) = \tau_p; \tau(z_i = -L/2) = 0. \tag{40}$$

Notice that after the first of these integration processes, all the functions required to define the $\gamma G_a(t)$ gradient profile (Eq. (34)) become known. Finally, the last step in deriving the RF offset profile to be used in the experiment, requires inverting $\tau(z)$ into $z(\tau)$, and plugging the result into $O(\tau) = \gamma G_e z(\tau) + \Omega_{inh}[z(\tau)]$.[4]

From an experimental standpoint, it is often simpler to program the resulting pulse as a phase table $\phi_{RF}(\tau)$, to be read at a constant dwell $\Delta\tau$ by the spectrometer's RF generation hardware. Moreover, since the inhomogeneity will in general affect the rate at which the RF sweeps any given range of frequencies, it also follows that the *amplitude* of the RF may have to be tailored during the clocking out of the pulse. Indeed as mentioned earlier (and as derived in the Appendix of Ref. 17), the strength γB_1 of a chirped pulse that is swept at a constant rate R can be calibrated so as to impart a (non-adiabatic) $\pi/2$ nutation of the spins. This in turn requires setting $\gamma B_1 \approx 0.25\sqrt{|R|}$, which is a constant for the homogeneous-field scenario. In the inhomogeneous field situation by contrast the sweep rate $R = \mathrm{d}O/\mathrm{d}\tau$ is no longer constant, and hence spins positioned at different z coordinates will be nutated by different extents unless the B_1 field is suitably compensated for this. This can be simply done by setting a second, amplitude-modulating table as part of the pulse definition with $\gamma B_1(\tau)$ defined as $0.25\sqrt{|\mathrm{d}O(\tau)/\mathrm{d}\tau|}$; not accounting for this leads to image distortions, as further illustrated below.

3.2. Limitations of the compensation procedure

Having derived the conditions under which the spatial encoding protocol can compensate for 1D field inhomogeneities, it is pertinent to discuss what will be the limits of such procedure. Some of these may arise from non-coherent decay factors (T_2, diffusion, motions) that will not be here addressed. But we have also identified two main methodological limitations worth discussing. One of these arises from our demand that the $\tau(z)$ in Eq. (39) be invertible into a $z(\tau)$ expression. Numerical simulations for various arbitrary $\Omega_{inh}(z)$ profiles reveal a variety of instances where, for large enough inhomogeneities, this is no longer possible.[5] In principle one should be able to accommodate the profile requested by the compensation as long as $\omega(z)$ is a univalued function, where each z voxel can be addressed independently and at will by an RF pulse of duration τ_p. This in turn requires that $\mathrm{d}\omega(z)/\mathrm{d}z \neq 0$ throughout the

[4] It appears that in the small inhomogeneity limit $|\mathrm{d}\Omega_{inh}(z)/\mathrm{d}z| \ll |\gamma G_e|$, replacing in Eq. (39) $\frac{\mathrm{d}\phi_e(z)}{\mathrm{d}z}/[\gamma G_e + \frac{\mathrm{d}\Omega_{inh}(z)}{\mathrm{d}z}]$ by $(\mathrm{d}\phi_e(z)/\mathrm{d}z)[1 - \frac{\mathrm{d}\Omega_{inh}(z)/\mathrm{d}z}{\gamma G_e}]/\gamma G_e$ could further aid in the calculations, even if we have not exploited this so far.

[5] Many of these cases actually reflect our reliance on a continuous frequency-swept pulse for achieving the desired $\phi_{RF}(\tau)$ pattern, which although a natural choice for implementing the encoding under homogeneous field conditions may no longer be optimal in the presence of field inhomogeneities. In such instances other excitation/inversion algorithms [29–31], might be more useful generators of the arbitrary profiles being sought.

course of the encoding; assuming that the inhomogeneity gradients we are dealing with are smaller than the γG_e gradient,[6] this translates into requesting

$$|\gamma G_e| > \left|\frac{d\Omega_{inh}(z)}{dz}\right| \forall z \in (-L/2, L/2). \quad (41)$$

A second, physically different limitation to the method described in the previous Paragraph is posed by the effects that will be introduced by $\Omega_{inh}(z)$ during the course of the acquisition, which entailing a time T_a that is usually longer than τ_p may eventually control the maximum limits of tolerable inhomogeneities. These longer-term distortions are mathematically represented by the *multiple* $z_{k(t)}$ roots that for long enough acquisition times t, will be able to satisfy the condition stated in Eq. (30). Indeed, when considering in this equation k and t as fixed parameters, one realizes that the signal detected at any given time will contain contributions from all z coordinates fulfilling the stationary phase condition

$$\frac{d\phi_e(z)}{dz} + \frac{d\Omega_{inh}(z)}{dz} \cdot t + k = 0. \quad (42)$$

In the $\Omega_{inh} = 0$ case $\phi_e(z)$ is a second-degree polynomial, and thus only a single z_k value (Eq. (12)) satisfies this condition. By contrast when $\Omega_{inh}(z) \neq 0$ then also $(d^3\phi_e/dz^3) \neq 0$, and the stationary phase condition may exhibit multiple roots. One of these will of course derive from the undistorted $z(t) = L/2 - L/T_a t$ solution for which ϕ_e and G_a were originally designed; but eventually other positions may end up satisfying Eq. (42), putting an end to the method's ability to deliver undistorted images. Fig. 8 illustrates with a series of graphs, the appearance of this multiple-roots phenomenon. Ways to deal with this problem reside in either setting all conditions such that the undesired stationary-phase voxels fall *outside* the FOV of the object that has been excited, or alternatively so that they only begin to appear at virtual times $t > T_a$. Multiple experimental parameters (G_e, G_a, τ_p, and T_a) are available to achieve these goals, as further illustrated in the following Paragraph.

3.3. One-dimensional compensations: an analytical example

Before proceeding with an extension of the protocol just presented to multidimensional cases, we deem it valuable to illustrate the implementation of the various calculations in the paragraphs above in an explicit derivation of the compensating functions $\phi_{RF}(\tau)$ and $G_a(t)$. Since, as mentioned earlier, spatially-encoded voxels are free from distortions upon being subject to linear field inhomogeneities, we shall consider towards this end a quadratic inhomogeneity

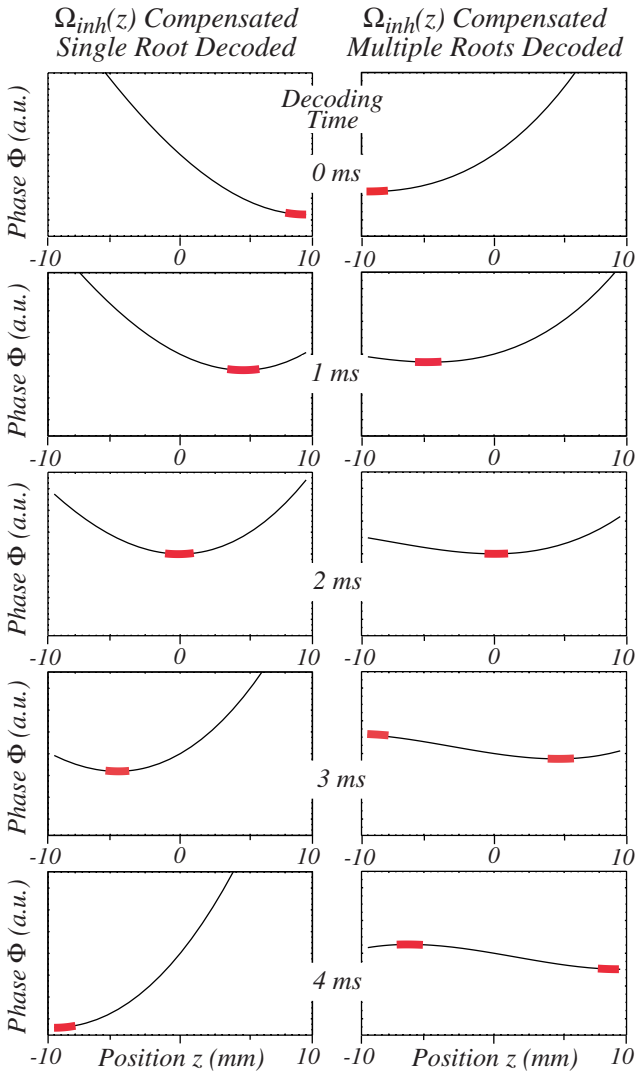

Fig. 8. Graphical explanation of how the onset of multiple roots may limit our proposed method of spatially-encoded field compensation. Shown on the left- and right-hand columns are numerically calculated profiles describing the evolution of phase encoded within a $-9 \leqslant z \leqslant 9$ mm long sample, as a function of the data acquisition time. In both cases the samples were assumed to have been excited with 4 ms long $\pi/2$ chirped pulses and constantly subject to an inhomogeneity $\Omega_{inh}(z) = 1.4z^2$ (in kHz and mm); an encoding gradient $G_e = -9.4$ G/cm was used in the left-column case while $G_e = +9.4$ G/cm for the right-hand scenario. The compensating algorithm described in the text was used in both instances, leading to detectable signals corresponding to the stationary-phase voxels indicated in all graphics by the thicker red traces. Notice that whereas in both cases the algorithm leads to an unraveling of the sample that proceeds, as desired, linearly in time, longer evolution times lead in the right-hand column to the appearance of a *second* region of flat phase whose signal will also contribute to the FID. As detailed in the text and illustrated in this Figure, such artifacts can be avoided by a judicious (and not necessarily harsher) choice of the encoding/decoding conditions.

$$\Omega_{inh}(z) = \eta_0 + \eta_1 z + \eta_2 z^2. \quad (43)$$

From the constant-voxel condition in Eq. (37) it follows that

$$\frac{d^3\phi_e(z)}{dz^3} = -2\eta_2 \frac{T_a}{L}. \quad (44)$$

[6] Another interesting alternative, dealing with exploiting this paper's approach to retrieve undistorted spatial images for cases where the gradient is actually *smaller* than the intrinsic inhomogeneities, will be discussed elsewhere.

This condition can be integrated twice subject to the boundary conditions in Eqs. (39) and (40) cast as

$$\tau(z_i)=0 \Longleftrightarrow \left.\frac{\mathrm{d}\phi_e}{\mathrm{d}z}\right|_{z_i=-L/2}=0; \tau(z_f)=\tau_p \Longleftrightarrow \left.\frac{\mathrm{d}\phi_e}{\mathrm{d}z}\right|_{z_f=L/2} = \left[\gamma G_e+\left.\frac{\mathrm{d}\Omega_{inh}(z)}{\mathrm{d}z}\right|_{z_f=L/2}\right]\tau_p$$

yielding an explicit form for the gradient to be applied over the course of the acquisition:

$$\gamma G_a(t)=-\eta_1-\frac{\gamma G_{eff}\tau_p}{T_a}-\frac{\eta_2 L\tau_p}{T_a}-\frac{2L}{T_a}\eta_2\cdot t, \tag{46}$$

where $\gamma G_{eff}=\gamma G_e+\eta_1$. This solution clearly reverts to the homogeneous demand $G_a=-G_e\tau_p/T_a$ on making $\Omega_{inh}(z)=0$, and entails otherwise a linear "increase" in gradient strength with time in order to account for progressive effects of the quadratic inhomogeneity. An interesting feature to remark regarding Eq. (46), is that in the inhomogeneous case it leads to a second solution in addition to $z(t)=L/2-L/T_a t$. This is a second root of the kind introduced earlier, which in this case will be expressed by

$$z_{artifact}(t)=\frac{\gamma G_{eff}\tau_p}{\eta_2 T_a}-\frac{L}{2}\left(1+\frac{2\tau_p}{T_a}\right)-\frac{L}{T_a}\cdot t. \tag{47}$$

Notice that just as the "legitimate" solution being sought, this position is also decoded linearly with time. This in turn enables one to avoid its interfering effects, by making sure that the different parameters making up the constant term of this position already place $z_{artifact}(t=0)$ outside the object's FOV. Fig. 9 illustrates an example of this carried out, in this instance by a judicious choice of the sign of the G_e gradient chosen for the encoding. Alternative routes of dealing with this kind of artifact are also conceivable.

The conclusion given earlier also indicated how double integration of Eq. (44) bound to Eq. (45), enables one to derive the tailored offset chirp to be applied for avoiding the dephasing effects introduced by the inhomogeneity. For the case of a quadratic $\Omega_{inh}(z)$ this can be carried out analytically and, following some algebra, leads to

$$O(\tau)=-\eta_o-\frac{\gamma G_{eff}[-2L\eta_2\tau+\tau_p(\gamma G_{eff}+L\eta_2)-\Delta]}{2\eta_2 T_a}+\frac{[2L\eta_2\tau-\tau_p(\gamma G_{eff}+L\eta_2)+\Delta]}{4\eta_2 T_a^2}, \tag{48a}$$

where

$$\Delta=\sqrt{(\gamma G_{eff}\tau_p-2L\eta_2\tau+L\eta_2\tau_p)^2+\eta_2 T_a[2L\gamma G_{eff}(\tau_p-2\tau)+L^2\eta_2(2\tau_p+T_a)]}. \tag{48b}$$

From here the tailored RF amplitude $\gamma B_1(\tau)$, proportional to $\sqrt{|\mathrm{d}O(\tau)/\mathrm{d}\tau|}$, can also be worked out. Fig. 9C illustrates the relevance of suitably tailoring this nutation, with an image decoded using all the right compensation parameters except for such RF amplitude correction.

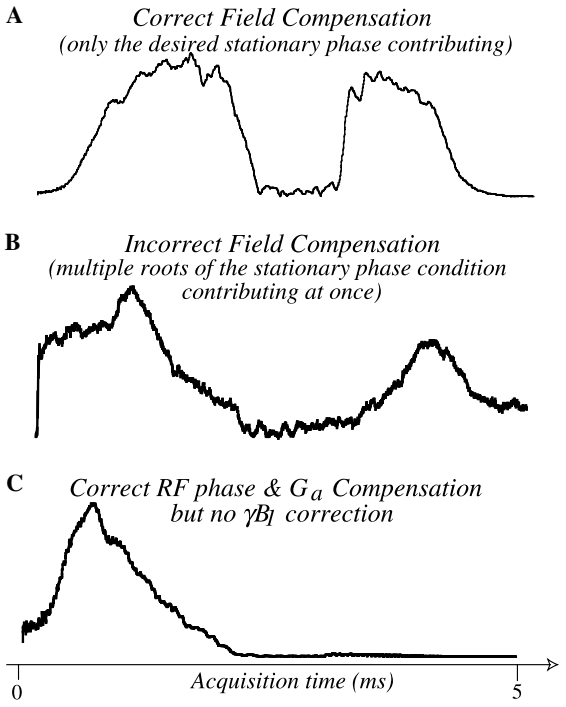

Fig. 9. Experimental illustration of different artifacts affecting the field-compensating principles described in this work, collected under the conditions depicted in Fig. 7 for the same 1D phantom. (A) Spatially-encoded profile obtained upon employing a "correct" excitation gradient ($G_e=5$ G/cm) as well as the RF and acquisition gradient shapes arising from the $\Omega_{inh}(z)$ profile. (B) Idem as (A) but upon choosing the opposite excitation gradient ($G_e=-5$ G/cm) and then solving for the correct compensating conditions. Notice the severe distortions arising due to the presence of multiple voxels satisfying the stationary phase condition for most of the acquisition time. (C) Profile resulting upon employing the appropriate excitation/acquisition gradients and RF offset shaping, but neglecting a suitable correction of the $\gamma B_1(\tau)$ RF amplitude.

4. Compensating inhomogeneities in multiple dimensions

The compensation principles described in the previous Section for the case of 1D acquisitions can be expanded to multidimensional single-scan experiments. A main demand of these *n*D procedures is that suitable encoding and decoding sequences be devised, whereby each voxel $\boldsymbol{r}$ *is addressed independently and only once*, both during the initial excitation as well as during the latter acquisition stages. A one-to-one relation during the encoding is required in order to be able to compensate each $\Omega_{inh}(\boldsymbol{r})$ element in the field distribution. The analogous decoding demand derives from the fact that the protocol enables the correct compensation of $\Omega_{inh}(\boldsymbol{r})$ solely for a single acquisition time t, but not for multiple times. For instance 2D encoding schemes of the kind illustrated in Figs. 4C and D will be unable to compensate generic $\Omega_{inh}(x,z)$ 2D distributions, as they both address all elements positioned perpendicular to a particular x or z coordinate at once. Neither will decoding schemes such as the ones in Figs. 4C and D succeed in compensating 1D distortions along the x direction, as individually encoded coordinates along this axis are interrogated multiple times during the acquisi-

tion. In general, full compensation of an arbitrary inhomogeneity along n-dimensions will demand the use of an nD spatial-encoding pulse, followed by a continuous n-dimensional rasterization of the image. When viewed as a function of τ and t both the nD encoding and decoding processes regain in this fashion a one-dimensional character, and the various equations and conditions derived earlier can be re-applied.

The mathematics of a full 3D inhomogeneity compensation are quite involved, and their general treatment will be deferred to a subsequent publication. Still, we would like to exemplify some of the new issues that will arise even when dealing with the simplest of nD compensation cases. One feature that was absent in both the 1D inhomogeneous field treatment as well as in the homogeneous nD one—but which is a regular feature of all $\Omega_{\text{inh}}(\boldsymbol{r})$ nD compensation schemes—concerns the fact that spins will no longer be addressed along orthogonal directions. This will in turn shift the initial coordinate of the rasterization from its ideal position, and mix the constant-voxel and linear rasterization demands among all n dimensions. This feature can be appreciated by considering the nD stationary phase condition Eq. (27a), which will now become

$$\begin{aligned} k(t) &= -\nabla_{\boldsymbol{r}}[\phi_{\text{e}}(\boldsymbol{r})] - t\cdot\nabla_{\boldsymbol{r}}[\Omega_{\text{inh}}(\boldsymbol{r})] \\ &= -\nabla_{\omega}[\phi_{\text{e}}(\boldsymbol{r})]\cdot J(\boldsymbol{r}) - t\cdot\nabla_{\boldsymbol{r}}[\Omega_{\text{inh}}(\boldsymbol{r})] \end{aligned} \tag{49}$$

with

$$\nabla_{\omega}[\phi_{\text{e}}(\boldsymbol{r})] = (\partial\phi_{\text{e}}/\partial\omega_x, \partial\phi_{\text{e}}/\partial\omega_y \partial\phi_{\text{e}}/\partial\omega_z)$$

and

$$\boldsymbol{J} = \begin{pmatrix} \partial\omega_x/\partial x & \partial\omega_x/\partial y & \partial\omega_x/\partial z \\ \partial\omega_y/\partial x & \partial\omega_y/\partial y & \partial\omega_y/\partial z \\ \partial\omega_z/\partial x & \partial\omega_z/\partial y & \partial\omega_z/\partial z \end{pmatrix} \tag{50}$$

the Jacobian matrix relating positions $\boldsymbol{r}$ and axes of frequency encoding $\boldsymbol{\omega}$. In the absence of inhomogeneities this transformation would be diagonal, with each frequency-swept encoding addressing its respective spatial direction. Yet in the presence of an $\Omega_{\text{inh}}(\boldsymbol{r})$ term $\boldsymbol{J}$ will connect the decoding along a given axis with encodings which happened along other, non-orthogonal directions. Also the conditions that define the constant voxel size will now require that conditions along multiple orthogonal directions be suitably related. Indeed for the inhomogeneous-field case we shall demand, in analogy to Eq. (36), that

$$\frac{\mathrm{d}}{\mathrm{d}t}[\det Q_{\boldsymbol{r}=\boldsymbol{r}(t)}] = 0 \tag{51}$$

where following Eq. (28) we define

$$\begin{aligned} \boldsymbol{Q}_{ij} &= \boldsymbol{D}_{ij}[\phi_{\text{e}}(\boldsymbol{r}) + \boldsymbol{k}\cdot\boldsymbol{r} + t\Omega_{\text{inh}}(\boldsymbol{r})] \\ &= \partial/\partial i\partial/\partial j\{\phi_{\text{e}}[\boldsymbol{\omega}(\boldsymbol{r})]\} + t\partial/\partial i\partial/\partial j[\Omega_{\text{inh}}(\boldsymbol{r})] \end{aligned} \tag{52}$$

Once again the Jacobian relating the encoding frequencies $\boldsymbol{\omega}$ and orthogonal directions $\boldsymbol{r}$ will intervene in this matrix via the derivatives of $\phi_{\text{e}}[\boldsymbol{\omega}(\boldsymbol{r})]$, making $\mathbf{Q}$ off-diagonal as long as $\Omega_{\text{inh}} \neq 0$.

Rather than considering such full treatment we shall focus here on the simpler case, of how to compensate a 2D spatially-encoded experiment for a 1D inhomogeneity of the type $\Omega_{\text{inh}}(z)$. Specifically we shall consider the 2D spin encoding instance illustrated in Fig. 4C, which will lead to

$$\phi_{\text{e}} = \phi_{\text{e}}^{x}(\omega_x)\phi_{\text{e}}^{z}(\omega_z) \tag{53}$$

now defined as a function of the swept-the RF encoding frequencies

$$\omega_z(z) = \gamma G_{\text{e}}^{z} z + \Omega_{\text{inh}}(z) \tag{54}$$

and

$$\omega_x(x,z) = \gamma G_{\text{e}}^{x} x + \Omega_{\text{inh}}(z). \tag{55}$$

Whereas the encoding will be imparted as a function of these frequency variables $\boldsymbol{\omega}$, the decoding process will still be given by gradients acting along orthogonal directions $\boldsymbol{r}$. A decision is thus to be made in terms of choosing a set of variables for describing the experiment: either for $\boldsymbol{r}$ or for $\boldsymbol{\omega}$. Going for the former implies rewriting the stationary phase condition in Eq. (27) as

$$\begin{aligned} (k_x, k_z) = &-(\partial\phi_{\text{e}}^{x}/\partial\omega_x, \partial\phi_{\text{e}}^{z}/\partial\omega_z + t\mathrm{d}\Omega_{\text{inh}}/\mathrm{d}z)\cdot \\ &\times \begin{pmatrix} \gamma G_{\text{e}}^{x} & \mathrm{d}\Omega_{\text{inh}}/\mathrm{d}z \\ 0 & \gamma G_{\text{e}}^{z} + \mathrm{d}\Omega_{\text{inh}}/\mathrm{d}z \end{pmatrix}, \end{aligned} \tag{56}$$

where as adumbrated the Jacobian matrix is involved on the right-hand side. On these $\boldsymbol{k}$ elements we shall once again impose the conditions that force an idealized rasterization of the image, which for trajectories zigzagging through the (x,z) plane can be cast analytically as

$$x(t) = x_i + L_x/2\cos\left[\frac{2\pi N_x}{T_{\text{a}}}(t+\Delta)\right]; \quad z(t) = L_z/2 - L_z/T_{\text{a}}t \tag{57}$$

N_x being the number of zigzags chosen. The appearance here of the new parameters x_i, Δ reflect the fact that, even if a π-driven encoding solely along the $\hat{x}$ axis is employed, the inhomogeneity will shift the rasterization away from zero and begin it at $x_i = -\frac{\Omega_{\text{inh}}(L_z/2)}{\gamma G_{\text{e}}^{x}}$. As in the 1D case Eq. (56) will have to be derivatized with respect to time in order to extract the acquisition gradients $G_{\text{a}}^{x}(t)$ and $G_{\text{a}}^{z}(t)$. Given the one-to-one relation between t and z (Eq. (57)) this is equivalent to taking a derivative with respect to z. Notice that this one-to-one relation is an important demand that could not have been fulfilled if considering the orthogonal x axis (of which t in Eq. (57) is not a single-valued function), thus giving mathematical expression to the physical demands with which we began this Section. Notice as well that since in the general case Ω_{inh}, $\phi_{\text{e}}^{x}(\omega_x)$ and $\phi_{\text{e}}^{z}(\omega_z)$ will be high-dimensional polynomials of x and z, we shall once again have to deal here with the possibility of multiple root solutions of the kind introduced in the previous Section.

Also as in the unidimensional case, the set of second-order spatial derivatives of $\phi_{\text{e}}(x,z)$ that are needed for defining the acquisition gradients $G_{\text{a}}^{x}(t)$, $G_{\text{a}}^{z}(t)$ can be retrieved

from the constant voxel condition. According to Eqs. (51) and (52) this will now require finding the determinant of the matrix

$$\mathcal{Q} = \begin{pmatrix} \left(\gamma G_e^x\right)^2 \frac{\partial^2 \phi_e^x}{\partial x^2} & \gamma G_e^x \frac{d\Omega_{inh}}{dz} \frac{d^2\phi_e^z}{d\omega_z^2} \\ \gamma G_e^x \frac{d\Omega_{inh}}{dz} \frac{d^2\phi_e^x}{d\omega_x^2} & \left(\gamma G_e^z\right)^2 \frac{d^2\phi_e^z}{dz^2} + 2\gamma G_e^z \frac{d\Omega_{inh}}{dz} \frac{d^2\phi_e^z}{d\omega_z^2} + \nabla^2\phi_e\left(\frac{d\Omega_{inh}}{dz}\right) + (\nabla_\omega \phi_e \cdot 1 + t)\frac{d^2\Omega_{inh}}{dz^2} \end{pmatrix}, \tag{58}$$

then setting its time- (i.e., its z-) derivative to zero, and looking for the appropriate ϕ_e^x, ϕ_e^z solutions. It can be shown that for the present case this becomes equivalent to demanding

$$\frac{d}{dt}\left\{\left(\frac{d^2\phi_e^x}{d\omega_x^2}\right)\left[\frac{d^2\phi_e^z}{dz^2} + \left(t + \frac{d\phi_e^x}{d\omega_x}\right)\frac{d^2\Omega_{inh}}{dz^2}\right]\right\} = 0. \tag{59}$$

Notice that the bracketed term in this derivative is akin to a product among the second-derivatives defining the Δx and Δz spatial resolutions, distorted as they now are by the effects of the inhomogeneity. A simple way to solve for the multiple mixed derivatives posed by this equation is to carry out the ω_x–encoding by means of a linear frequency sweep—for instance via an adiabatic π sweep leading to $\phi_e^x(\omega_x) = c_x\omega_x^2$—and port all the necessary corrections to a tailored encoding solely along the z axis. This shifts all the focus onto the $\Delta z^{-1} \approx \lfloor \frac{d^2\phi_e^z}{dz^2} + (t + \frac{d\phi_e^x}{d\omega_x})\frac{d^2\Omega_{inh}}{dz^2} \rfloor$ term of Eq. (59); setting this to zero we can derive the requirement

$$\frac{d^3\phi_e^z}{dz^3} = -\frac{d}{dz}\left\{\frac{d^2\Omega_{inh}}{dz^2}\left[t(z) + 2c_x\gamma G_e^x \cdot x[t(z)]\right] + 2c_x\Omega_{inh}(z)\right\}. \tag{60}$$

This is the 2D analog to Eq. (37) and can likewise be integrated to obtain $\frac{d^2\phi_e^z}{dz^2}$ based on the boundary conditions applying to the relations given in Eq. (57) for $x(t)$ and $z(t)$; from here the remainder of the reconstruction procedure can be continued backwards, along lines similar to those detailed for the unidimensional case.

Based on the resulting relations a software package capable of providing the encoding RF profile $\phi_{RF}[\tau(z)]$ and decoding gradient $G_a^z(t)$ needed for correcting an $\Omega_{inh}(z)$ inhomogeneity affecting a $\pi/2(z) - \pi(x)$ encoding experiment was written; as mentioned, even in such 2D scenario all G_e gradients as well as the x-related functions $\phi_{RF}[\tau(x)]$ and $G_a^x(t)$ could be left out of the correcting task. Experiments were then carried out based on the zigzagging rasterization in Eq. (57), for the sake of testing the capabilities of the ensuing compensation. Fig. 10 illustrates a set of representative results obtained in this fashion. Illustrated in panels A and B are single-scan 2D MRI profiles obtained on a 5 mm water phantom in the absence of inhomogeneities utilizing EPI and spatial-encoding approaches; both images are comparable, even if the former is of a slightly higher definition. Shown in Figs. 10C and D is an analogous comparison but upon subjecting the sample to a ca. 2.5 kHz inhomogeneity artificially induced by de-shimming the sample along the z axis; both images are severely distorted, as expected, along this weak-gradient read-out direction. Fig. 10E

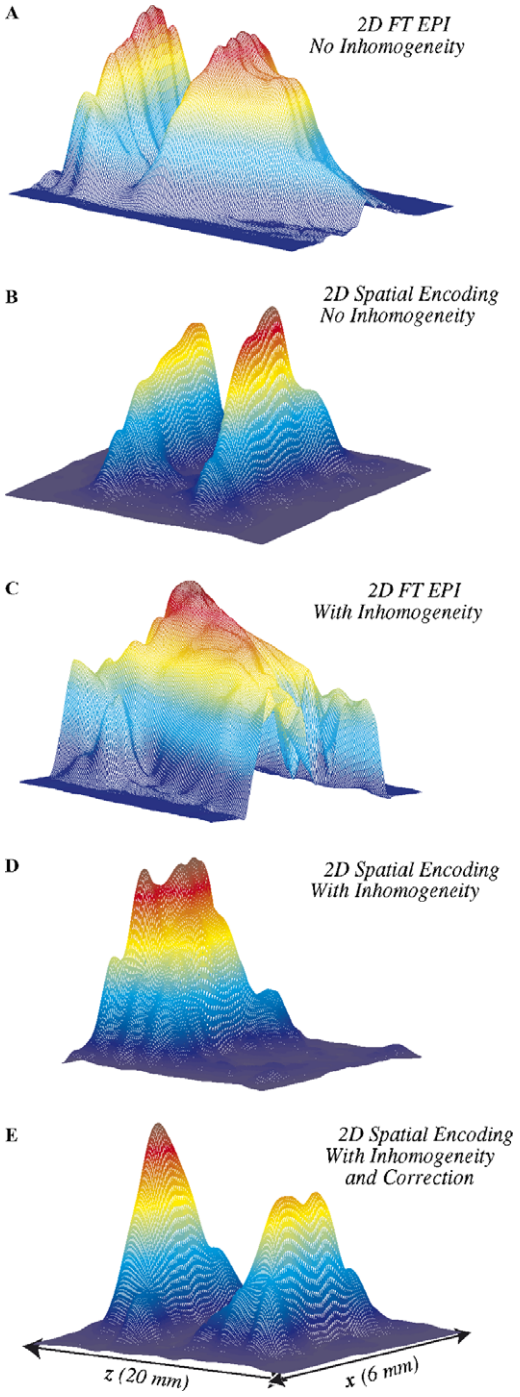

Fig. 10. Experimental demonstration of the field-compensating principles described in this work, for the case of a two-dimensional acquisition on the phantom sample introduced in Fig. 3. (A) Single-scan 2D FT EPI image recorded using a blipped read-out of 32 echoes spread over 32 ms; acquisition gradients were $G_a^x = \pm 15$ G/cm and $G_a^z = 0.85$ G/cm (pulsed over 50 μs every 950 μs). (B) Single-scan 2D spatially-encoded image collected using a zigzagging scheme as in Fig. 6A except for $G_e^x = G_e^z = 4$ G/cm; $G_a^x = \pm 25$ G/cm and $G_a^z = 0.5$ G/cm. (C and D) *Idem* as in (A and B) but upon subjecting the sample to the artificial $\Omega_{inh}(z)$ illustrated in Fig. 11A. (E) Idem as in (D) but after inserting the mapped inhomogeneity profile into the algorithm described in the text, calculating from it the correcting RF sweep and acquisition gradient patterns, and applying it for the acquisition of the data. Fig. 11 depicts the main parameters involved in this correction, as well as a comparison between the raw data sets arising with and without such compensation.

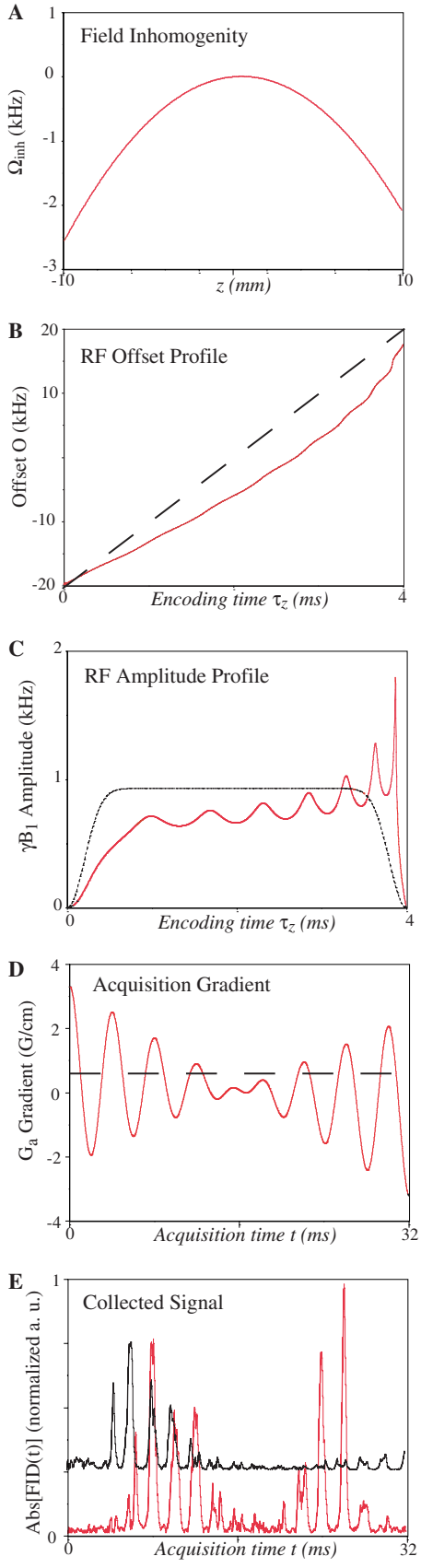

illustrates the recovery potential of the spatial encoding approach upon applying the compensation just described; as can be appreciated, the quality of the resulting 2D image is not significantly different from that of its homogeneous-field analog in panel B. A few additional comparisons between un-corrected and corrected features worth remarking in this 2D procedure, are illustrated in Fig. 11.

5. Conclusions

By treating the sample in a non-uniform fashion, the spatial encoding protocol enables the acquisition of nD MR images within a single scan, while at the same time opening up various possibilities to deal with field inhomogeneities. The present study focused on compensating artifacts that arise from a B_0 field distribution; we shall discuss elsewhere additional opportunities that arise in terms of compensating B_1-related inhomogeneities, for dealing with the presence of multiple chemical sites, as well as for removing artifacts that arise from the combined action of all of these factors. As for the specific B_0 compensation procedures described in this work, we believe that while many of their principles will remain valid, their implementation could be improved over the particular set of choices made in the experiments and calculations hereby presented. In particular it is not clear that the ways we have employed swept RF pulses represent the best necessary route to achieve the desired $\phi_{RF}(r)$ profiles, or that our choice to reintroduce the image ideality while keeping the encoding gradients and the acquisition dwell time constant is optimal. We are still in the process of exploring these various options, and of assessing their relative merits and performance.

Although significantly simpler and less general than its higher-dimensional counterpart, the one-dimensional B_0 compensation scheme hereby introduced could proof practical in a number of instances where field inhomogeneities are primarily relevant along one of the spatial directions, and where single-scan acquisitions are deemed necessary. These may include the read-out direction of a 2D EPI scan, or ex-situ single-sided imaging setups. In such cases the execution of a hybrid spatial-encoding/Fourier scheme of the type illustrated in Fig. 4B, where the small bandwidth axis would undergo a "blipped" incrementation and concomitant Ω_{inh}

Fig. 11. (B–D) Comparison between various parameters involved in the acquisition of the inhomogeneity-compensated image shown in Fig. 10E (red, full lines), and the ones that would have been used for an equivalent acquisition in the absence of inhomogeneities (black, dashed). The actual experiment involved a 2D spatially-encoded sequence utilizing a zigzag decoding (Fig. 4C) with $N_2 = 8$, and assumed FOVs = 23 mm (z) × 6 mm (x). Both encoding gradients were set at 4 G/cm and encoding times at 4 ms; the field inhomogeneity shown in (A) was mapped and assumed in the compensation calculations. (E) shows a comparison between the time-domain data arising in the presence of the inhomogeneity if the compensation procedure is (red lower trace) or is not (black upper trace) used. Notice here the ability of the compensation to "revive" the signal, extending it far beyond its effective T_2^*.

field compensation while FIDs are actually digitized while under the action of a strong orthogonal *k*-space encoding, could offer several of the advantages while avoiding the comparative disadvantages of spatially-encoded MRI. Furthermore, the spatially selective nature of this procedure also makes it particularly well suited to spatially discriminating detection setups, such as those arising in parallel imaging [32,33]. Combining the scheme hereby discussed with other EPI-derived inhomogeneity compensation procedures [34,35] is also an avenue worth pursuing. Further tests of these various options are currently in progress.

Acknowledgments

This work was supported by the Israel Science Foundation (ISF 1206/05) and by the Horowitz Fund (project 531/1).

References

[1] F. Schmidt, M.K. Stehling, R. Turner, Echo Planar Imaging: Theory, Technique and Application, Springer Verlag, Berlin, 1998.
[2] M.A. Bernstein, K.F. King, X.J. Zhou, Handbook of MRI Pulse Sequences, Academic Press, San Diego, 2004.
[3] R.B. Buxton, An Introduction to Functional MRI: Principles and Techniques, Cambridge University Press, Cambridge, 2001.
[4] P. Mansfield, Multi-planar image formation using NMR spin echoes, J. Phys. C: Solid State Phys. 10 (1977) 55–58.
[5] A. Haase, Snapshot FLASH MRI, applications to T1, T2 and chemical-shift imaging, Magn. Reson. Med. 13 (1990) 77–89.
[6] I.J. Lowe, R.B. Wysong, DANTE ultrafast imaging sequence (DUFIS), J. Magn. Reson. B 101 (1993) 106–109.
[7] J. Jeener, Lecture presented at Ampere International Summer School II, Basko Polje, Yugoslavia, September 1971.
[8] W.P. Aue, E. Bartholdi, R.R. Ernst, Two dimensional spectroscopy, Application to nuclear magnetic resonance, J. Chem. Phys. 64 (1976) 2229–2246.
[9] D.B. Twieg, The k-trajectory formulation of the NMR imaging process with applications in analysis and synthesis of imaging methods, Med. Phys. 10 (1983) 610–621.
[10] M. Doyle, R. Turner, M. Cawley, P. Glover, G.K. Morris, B. Chapman, R.J. Ordidge, R. Coxon, R.E. Coupland, B.S. Worthington, P. Mansfield, Real time cardiac imaging of adults at video frame rates by magnetic resonance imaging, Lancet 2 (1986) 682–683.
[11] C.B. Ahn, J.H. Kim, Z.H. Cho, High speed spiral scan echo planar imaging, IEEE Trans. Med. Imaging 5 (1986) 2–5.
[12] K. Oshio, D.A. Feinberg, GRASE imaging: a novel fast MRI technique, Magn. Reson. Med. 20 (1991) 344–349.
[13] L. Frydman, T. Scherf, A. Lupulescu, The acquisition of multidimensional NMR spectra within a single scan, Proc. Natl. Acad. Sci. USA 99 (2002) 15858–15862.
[14] L. Frydman, T. Scherf, A. Lupulescu, Principles and features of single-scan two-dimensional NMR spectroscopy, J. Am. Chem. Soc. 125 (2003) 9204–9217.
[15] Y. Shrot, L. Frydman, Single-scan NMR spectroscopy at arbitrary dimensions, J. Am. Chem. Soc. 125 (2003) 11385–11396.
[16] L. Frydman, Single-scan multidimensional NMR, Compts. Rends. Chemie. 9 (2006) 336–345.
[17] Y. Shrot, L. Frydman, Spatially encoded NMR and the acquisition of 2D magnetic resonance images within a single scan, J. Magn. Reson. 172 (2005) 179–190.
[18] B. Shapira, L. Frydman, Spatial encoding and the acquisition of high-resolution NMR spectra in inhomogeneous magnetic fields, J. Am. Chem. Soc. 126 (2004) 7184–7185.
[19] D. Topgaard, R.W. Martin, D. Sakellariou, C.A. Meriles, A. Pines, "Shim pulses" for NMR spectroscopy and imaging, Proc. Natl. Acad. Sci. USA 101 (2004) 17576–17581.
[20] D. Kunz, Use of frequency-modulated RF pulses in MR imaging experiments, Magn. Reson. Med. 3 (1986) 377–384.
[21] D. Kunz, Frequency-modulated RF pulses in spin-echo and stimulated-echo experiments, Magn. Reson. Med. 4 (1987) 129–136.
[22] J.G. Pipe, Spatial encoding and reconstruction in MRI with quadratic phase profiles, Magn. Reson. Med. 33 (1995) 24–33.
[23] J.G. Pipe, Analysis of localized quadratic encoding and reconstruction, Magn. Reson. Med. 36 (1996) 137–146.
[24] A. Tal, B. Shapira, L. Frydman, A continuous phase-modulated approach to spatial encoding in ultrafast 2D NMR spectroscopy, J. Magn. Reson. 176 (2005) 107–114.
[25] N.S. Andersen, W. Kockenberger, A simple approach for phase-modulated single-scan 2D NMR spectroscopy, Magn. Reson. Chem. 43 (2005) 795–797.
[26] J.I. Jackson, C.H. Meyer, D.G. Nishimura, A. Macovski, Selection of a convolution function for Fourier inversion using gridding, IEEE Trans. Med. Imaging 10 (1991) 473–478.
[27] P. Jezzard, R.S. Balaban, Correcting for geometric distortions in echo planar images from B_0 variations, Magn. Reson. Med. 34 (1995) 65–73.
[28] P. Irarrazabal, C.H. Meyer, D.G. Nishimura, A. Macovski, Inhomogeneity correction using an estimated linear field map, Magn. Reson. Med. 35 (1996) 278–282.
[29] M. Shinnar, H. Eleff, H. Subramanian, J.S. Leigh, The synthesis of pulse sequences yielding arbitrary magnetization vectors, Magn. Reson. Med. 12 (1989) 74–80.
[30] J.M. Pauly, P. LeRoux, D.G. Nishimura, A. Macovski, Parameter relations for the Shinnar–LeRoux selective excitation pulse design algorithm, IEEE Trans. Med. Imaging 10 (1991) 53–65.
[31] R.F. Schulte, J. Tsao, P. Boesiger, K.P. Pruessmann, Equiripple design of quadratic-phase RF pulses, J. Magn. Reson. 166 (2004) 111–122.
[32] K.P. Pruessmann, M. Weiger, M.B. Scheidegger, P. Boesiger, Sense: sensitivity encoding for fast MRI, Magn. Reson. Med. 42 (1999) 952–962.
[33] D.K. Sodickson, C.A. McKenzie, A generalized approach to parallel magnetic resonance imaging, Med. Phys. 28 (2001) 1629–1643.
[34] K.-D. Merboldt, J. Finsterbusch, J. Frahm, Reducing inhomogeneity artifacts in functional MRI of human brain activation—thin sections vs gradient compensation, J. Magn. Reson. 145 (2000) 184–191.
[35] V.A. Stenger, F.E. Boada, D.C. Noll, 3D tailored RF pulses for the reduction of susceptibility artifacts in T2-weighted functional MRI, Magn. Reson. Med. 44 (2000) 525–531.